Enhancing catalytic activity of tungsten disulfide through topology

Longlu Wang[a,1], Gang Zhou[b,1], Hong Luo[c,1], Qingfeng Zhang[a], Jue Wang[a], Chunwang Zhao[d], Apparao M. Rao[e], Bo Xu[f], Bingan Lu[a,*]

[a] School of Physics and Electronics, Hunan University, Changsha 410082, China
[b] Key Laboratory of Modern Acoustics, MOE, Institute of Acoustics and Collaborative Innovation Center of Advanced Microstructures, National Laboratory of Solid State Microstructures, Nanjing University, China
[c] College of Mechanical & Vehicle Engineering, Hunan University, Changsha 410082, China
[d] College of Science, Inner Mongolia University of Technology, Hohhot 010051, China
[e] Department of Physics and Astronomy, Clemson Nanomaterials Institute, Clemson University, Clemson, SC 29634, United States
[f] Department of Physics, Laboratory of Computational Materials Physics, Jiangxi Normal University, Nanchang 330022, China

ARTICLE INFO

ABSTRACT

Phase transition through local strain engineering is an exciting yet complex phenomenon in nanoscience for enhancing electronic, magnetic, and catalytic properties of nanomaterials. Here we report a topotactic transformation in 2H-WS_2 nanobelts into 1T-WS_2 nanohelices, which is mediated *via* an aqueous electrochemical activation method. The resulting nanohelices exhibited superior catalytic properties for HER with a low overpotential of 170 mV for an electrocatalytic current density of 10 mA/cm^2. Notably, the electrochemical stability of WS_2 nanohelices increased after 20,000 cycles, where the stability of the Pt benchmark catalyst is known to decrease, thus implying WS_2 nanohelices as ideal catalysts for long-term electrochemical processes. The emergence of such enhanced properties is attributed to the strain induced decrease in charge transfer resistance, enhanced per site activity and increased number of active edge sites in 1T-WS_2 nanohelices. This study points the way for creating topological motifs in 2D materials with novel properties.

1. Introduction

Topology is reshaping materials science and technology by providing blueprints that allow novel physical and chemical properties to be elicited in nanomaterials [1–3] and complex molecular architectures [4]. For example, the construction of diverse nanoscale topologies created *via* DNA nanotechnology has received considerable attention in the past decades [5]. However, it remains poorly studied in inorganic nanomaterials, most likely due to their reported topological invariance [6]. While researchers have extensively explored the catalytic properties of mesoporous architecture of noble metals and other inorganic compounds for years, little attention was paid to their geometric topologies [1–6] because of the daunting challenges in synthesis and the ability to modulate their topological motifs [7]. In this regard, *in situ* construction of topology-controlled nanostructures is an exciting approach for realizing catalytically active edge morphologies in transition metal dichalcogenides (TMDs).

Nanoribbons and nanobelts of 2D materials have gained much interest because of the unique properties associated with their low dimensionality [8]. A phase transition from the 2H to 1T phase occurs easily *via* gliding of the intra-layer S atomic plane in TMDs [9–12]. This first order phase transition is well known and related to electron transfer during Li or K intercalation into the MoS_2 layers [13]. However, it is difficult to control this phase transition because of the thermodynamic instability of the 1T phase, which reversibly switches to the 2H phase upon thermal annealing at 80 °C for metallic TMDs and impedes its practical application [14]. Therefore, from a thermodynamic standpoint, it is still a challenge to create a stable 1T-WS_2 phase. Thus, the exploration of new synthesis methods to prepare stable 1T-WS_2, and further precisely investigate their catalytic properties is highly desirable. Recently, Researchers are actively involved in elucidating new methods such as electron beam irradiation [15], and strain engineering [16]. It was also reported that the plasmonic hot electron [17], high mechanical pressure [10], sulfur vacancies [18] or supercritical CO_2 [19] can induce local phase transformation in TMDs. Interestingly, the presence of dopant impurities such as Au or Re was also shown to stabilize the 1T phase of WS_2. In essence, either charge injection or strain can led to a stable phase transition to 1T-WS_2.

---

* Corresponding author.
E-mail address: luba2012@hnu.edu.cn (B. Lu).
[1] These authors contributed equally to this work.

Here we discuss how a topological transformation of 2H-WS$_2$ nanobelts yields 1T- WS$_2$ nanohelices with enhanced catalytic activity in their basal plane surfaces, and enhanced electron transport between the active sites in 1T- WS$_2$ nanohelices and the electrodes. An intrinsic bending strain facilitates gliding of the intralayer plane that leads to the transversal displacement of the S plane from the 2H phase to form the 1T phase. The 1T-WS$_2$ nanohelices exhibited a high efficiency in the hydrogen evolution reaction (HER) with a rather low Tafel slope of ~40 mV dec^{-1} and a low overpotential of 170 mV for an electrocatalytic current density of 10 mA/cm^2.

2. Experimental section

2.1. Materials synthesis

Bottom-up synthesis: Hydrothermal reaction was used to synthesize WS$_2$ nanobelts in a sealed autoclave system. Ammonium tungstate hydrate ((NH$_4$)$_{10}$W$_{12}$O$_{41}$.xH$_2$O, AR) and thiourea (CS (NH$_2$)$_2$, AR) were commercially procured from Shanghai Chemical Reagent Co. Ltd. All reagents were analytical grade and used as-received without further purification. For the synthesis, 0.5 mmol of (NH$_4$)$_{10}$W$_{12}$O$_{41}$.xH$_2$O and 30 mmol of thiourea were dissolved in 35 mL of distilled water under vigorous stirring to form a homogeneous solution. Next, the solution was transferred into a 45 mL Teflon-lined stainless-steel autoclave, maintained at 220 °C for 72 h, and naturally cooled down to room temperature. The final black product was washed several times with absolute ethanol and dried at 60 °C under vacuum.

2.2. Characterization of materials

The TEM and HRTEM images and electron diffraction studies were performed on a FEI Tecnai G2 F20 S-Twin microscope operated at an accelerating voltage of up to 200 kV. The TEM samples were prepared by sonication at 500 W for ~5 min, and 25 μL of the supernatant was dropped onto holey carbon grids. The SEM images were obtained using a field-emission gun SEM (Quanta 400 FEG FEI). The fraction of each phase of WS$_2$ was quantified using x-ray photoelectron spectrometer (XPS, K-Alpha 1063, Thermo Fisher Scientific, England) equipped with an Al-Kα x-ray source.

2.3. Electrochemical performance

Electrochemical measurements were performed in a three-electrode electrochemical cell using an Autolab PGSTAT302 N potentiostat. All measurements were performed in 50 mL of 0.5 M H$_2$SO$_4$ (aq.) electrolyte (pH = 0.16) prepared using 18 M deionized water purged with Ar gas (99.999%). A glassy carbon electrode (CH Instruments, dia. ~3 mm) coated with WS$_2$ samples was employed as the working electrode and a saturated calomel electrode (SCE) (CH Instruments) was used as a reference electrode. A graphite rod (Alfa Aesar) was used as the counter electrode. A glassy carbon plate loaded with WS$_2$ samples was also employed as a working electrode to monitor the morphology change during potential cycling. Typically, 4 mg of WS$_2$ catalyst was suspended in 1 mL ethanol with 5 mL Nafion solution (5 wt.%, DuPont) to form a homogeneous ink assisted by ultrasound. Next, 25 μL of the ink was micro-pipetted, spread onto the surface of glassy carbon, and dried under room temperature. The final loading of the WS$_2$ catalysts on the working electrode was 0.5 mg cm^{-2}.

As a comparison, carbon-supported Pt (Pt/C, 20%, Alfa Aesar) was also tested under identical conditions with a Pt loading of 25 μg cm^{-2}. A magnetic stir bar was used during the electrochemical tests to improve the mass transport. The SCE was calibrated in high-purity H$_2$, and the electrolyte was stirred through saturated electrolyte using platinum as both the working and counter electrodes. Cyclic voltammetry was run at a scan rate of 1mVs^{-1}, and the average of the two potentials at which the current crossed zero was recorded as the thermodynamic

potential for the HER. All reported potentials are referenced to RHE. In 0.5 M H$_2$SO$_4$, E(RHE) = E(SCE) + 0.254 V. HER activity was measured using linear sweep voltammetry between +0.10 and −0.50 V versus RHE with a scan rate of 5mVs^{-1}. The stability was evaluated by the potential cycling performed using cyclic voltammetry initiating at +0.2 V and ending at −0.2 V versus RHE at either 100mVs^{-1} or 5mVs^{-1}. All data were corrected for a small ohmic drop measured by EIS.

2.4. DFT calculations

Structural relaxation was performed using DFT method as implemented in Venna ab initio simulation package (VASP) with a plane wave basis set. The projector-augmented wave (PAW) method was used for the electron–ion interaction. Generalized gradient approximation (GGA) with the Perdew–Burke–Ernzerhhof (PBE) exchange-correlation functional was adopted in the calculations. The cut-off energy of 550 eV was employed for the plane wave basis. The Brillouin zone (BZ) integration was sampled by 8 × 8×1 Monkhorst–Pack k-point for all structural optimization. The convergence criteria for total energies and ionic forces were set to be 10^{-8} eV and 10^{-5} eV Å^{-1} in the formula unit. The phonon frequencies were calculated by using PHONOPY code, which can directly use the force constant (Hessian matrix) calculated by DFT as also implemented in VASP.

The single-layered WS$_2$ was modeled using surface and edge supercells separated in the periodic direction by a 15 Å-thick vacuum slab. For the surface, the most stable H binding site in the basal plane of WS$_2$ is on top of the S atoms. For the edge, we have examined two possible sites with high symmetry S-top site and W-top site of H adsorption. The H coverage considered in the calculations is 6.25%. The free energy change for H* adsorption on WS$_2$ surface and edge (ΔG_{H*}) was calculated as follows, which is proposed by Norskov and coworkers [16]:

$$\Delta G_{H*} = E_{total} - E_{WS_2} - \frac{E_{H_2}}{2} + \Delta E_{ZEP} - T\Delta S$$

where E_{total} is the total energy for the adsorption state, E_{WS2} is the energy of pure surface or edge, E_{H2} is the energy of H$_2$ in the gas phase, ΔE_{ZEP} is the zero-point energy change and ΔS is the entropy change. Thus, (ΔE_{ZEP}-$T\Delta S$) is simplified as 0.27 eV, where 0.27 eV is the contribution from ZPE and entropy at 298 K.

3. Results and discussion

3.1. Anisotropic driving force induced topological transformations

It is well known that the charge transferring due to lithium intercalation in TMDs induce a first-order phase transition from the semiconducting 2H phase to the metallic 1T phase, where the 1T phase is obtained through the gliding of the S plane over a distance equivalent to a = 3.16 Å during the intercalation–exfoliation reactions. [14–19] The anisotropic driving force stems from an imbalance along different sides in this asymmetry shape [20,21]. Considering the unique nanoribbon structure with a strain gradient, TMDs can spontaneously bend and twist into a helix (topological transformation) when subjected to an anisotropic driving force. Strain induced by topotactic transformation may turn 2H-WS$_2$ nanobelts into efficient electrocatalysts for the hydrogen evolution reaction. Three atomic models were built to illustrate the different morphologies for the WS$_2$ catalyst (see Fig. 1). Mechanically stretching a WS2 nanobelt into a wrinkled sheet can be regarded as a prototypical method to induce shape anisotropy, thus enabling the possibility of thermodynamically inducing phase transition through mechanical deformation. [22–26].

The helical microscale architectures are formed through directional rolling which creates anisotropic mechanical stresses. The driving force for twisting may be asymmetric due to the preferential doping of WS$_2$
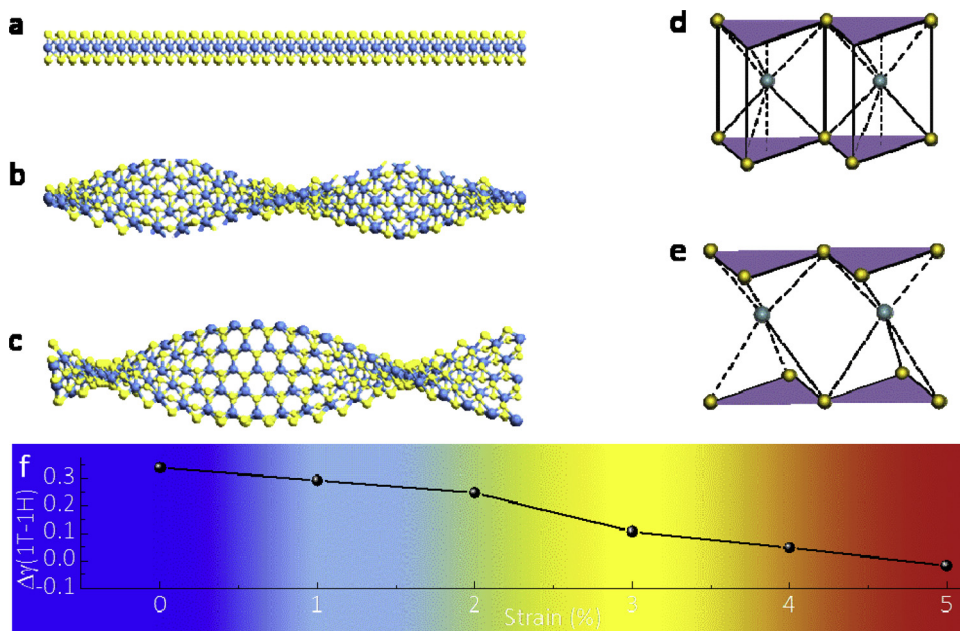
Fig. 1. | Strain induced topotactic transformation of WS2 nanobelts into nanohelices. The yellow and blue colored balls in a–e represent S and W atoms, respectively. Side views of an armchair-terminated (a) and twisted armchair WS2 nanobelt (b), and a helical WS2 nanowire (c). Panel (f) shows the calculated formation-energy difference $\Delta\gamma$ between the 2H (d) and 1T (e) phases as a function of strain. Clearly, the 1T -phase is more stable than the 2H phase when strain approaches 5%.

nanobelts with hydrogen and the asymmetric surface forces arising from local high surface energy. As calculated, the gain in surface energy from twisting is sufficient to compensate the mechanical tension due to curving. While thicker nanobelts are rigid and straight, the thinner nanobelts can be flexible and curved. Figs. 1a and S1a show respectively the side and end views of a nanobelt consisting of a S–W–S sandwich. Similar views of a twisted nanobelt (Figs. 1b and S1b) and a twisted nanowire (Figs. 1c and S1c) are also shown for comparison. Motivated by the above considerations, we hypothesize that the 1T phase of WS2 can be realized in WS2 nanohelices due to twist-induced gliding of atomic planes. As nanosheets self-assemble by morphing into nanohelices, a stabilizing energy for the 1T phase is attained due to the van der Waals interactions between layers when the external forces glide the S-plane to a maximum extent. Twisting the nanobelts into nanohelices results in a bending strain, and a consequent lattice distortion (Fig. 1e). In this state, the helices become unstable due to the strain, but the van der Waals force and the self-stabilizing energy of the helices, maintains this state. Thus, through a nondestructive *in situ* topotactic transformation, 2H-WS2 nanobelts can be engineered into stable 1T-WS2 nanohelices.

An engineered shape anisotropy, such as the one discussed above, can boost the number of catalytically active sites in WS2 nanohelices. [27–34] Moreover, the anisotropy also tunes the local charge distribution and the electronic work function which effectively minimizes the contact resistance between the WS2 basal plane and the electrodes, thus leading to enhanced catalytic activity compared to its flat cousin.

3.2. Self-optimizing hydrogen evolution catalytic activity of WS2 nanobelts

We successfully prepared WS2 nanobelts *via* a hydrothermal synthesis method that is based on a simple disproportionation reaction (Fig. S2). The electron microscope images and elemental analyses depicted in Fig. S2a–e suggest that the WS2 nanobelts prepared in this study were straight and predominantly of the 2H-phase. Our calculated phonon dispersion spectrum (Fig. S2f) further suggested that the WS2 2H phase is stable as no imaginary frequencies (soft modes) were found in our calculations. However, we found that the WS2 1T phase is indeed metastable with a maximum value of ˜ −4 THz of the imaginary frequency (Fig. S2g), consistent with previous reports in the literature. In particular, the WS2 1T phase is dynamically instable at the zone border with the largest instability around the K point of its hexagonal lattice. In

addition, we found that the imaginary frequencies mainly originate from two out of the three acoustic branches with a maximum value of ˜ −4 THz for the imaginary frequency. Last but not the least, anisotropic nanobelts are also envisaged as a model system which boosts the catalytic performance of the HER depicted in Fig. 2a. The catalytic activity of WS2 nanobelts improved with cycling, and such self-optimizing behavior has practical advantages compared with more complex approaches for optimizing WS2-based catalysts in that it enables highly scalable processing with minimal additional treatment. As expected, the Tafel slope for the WS2 nanobelts improved from 52 to 40 mV/dec after 10,000 CV cycles (Fig. 2b) suggesting that the HER could have proceeded *via* the Volmer–Heyrovsky mechanism, with the Heyrovsky step as the rate-determining reaction. Aside from a stringent requirement for high activity, an important parameter for viability of a HER catalyst is its electrochemical stability. Thus, the WS2 nanobelts were continuously cycled for more than 10,000 cycles in H_2SO_4 (0.5 M), and their electrocatalytic activity was periodically monitored by measuring the CV response after every 1000 potential cycles and then plotting the change in cathodic current density at -0.2 V versus the RHE (Fig. 2c). Under this condition, the cathodic current density increased initially and stabilized after a couple of thousands of potential cycles highlighting the remarkable stability of WS2 nanobelts over the course of 20,000 cycles. In particular, the HER activity of WS2 nanobelts after 10,000 cycles outperformed that of most WS2 based hybrid catalysts in terms of both the overpotential and Tafel slope (Table S1). It is worth mentioning that the HER activity of WS2 nanobelts after 10,000 cycles is comparable to that of other representative non-precious HER electrocatalysts in Table S2. [36–44]. Using gas chromatography the electrochemical results were correlated to the actual rates of H_2 production (Fig. S7), and the obtained Faradaic efficiency (FE) is near 100% (Table S3).

To gain insights into the fundamental basis for improved performance with cycling, we performed *in situ* Raman spectroscopy of WS2 nanobelts during the CV sweeps (Fig. 2d). The intensities of the Raman active modes exhibited by the 2H phase decreased with increasing CV cycles while the peaks corresponding to the 1T phase became sharper and prominent. X-ray photoelectron spectroscopy (XPS) (Fig. S3) further indicated a relative percentage of 1T-WS2 to 2H-WS2 as 70%:30%, respectively, which was deduced by integrating the area under the $W4f_{7/2}$ peak. We attribute the dramatic improvement in the electrochemical activation to a decreased charge transfer resistance that is
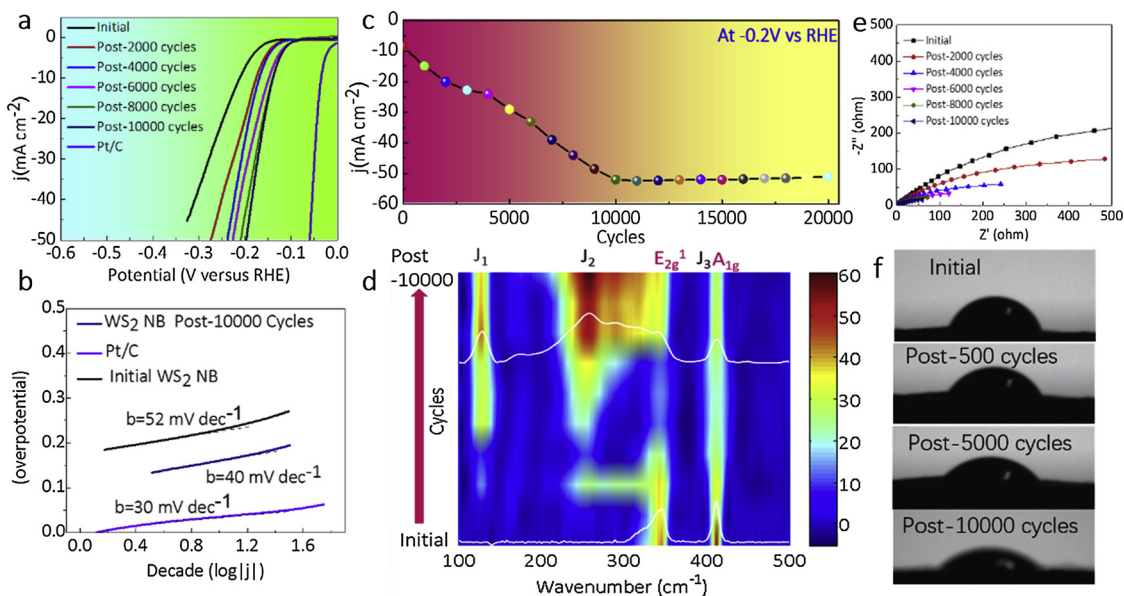
Fig. 2. (a) Electrochemical data of WS$_2$ nanobelts in H$_2$SO$_4$ (0.5 M). Polarization curves are shown as a function of number of potential cycles and compared to that of the Pt benchmark catalyst. (b) Corresponding Tafel plots of a WS$_2$ nanobelt, Pt/C and WS$_2$ nanobelt post-10,000 cycles. (c) Change in the HER cathodic current density (at −0.20 V *vs.* RHE) with the number of potential cycles. (d) *In situ* Raman spectroscopy as a function of CV cycles (phase transformation process). (e) Nyquist plots and (f) static contact angle along with the number of potential cycles.

brought about by a phase transformation to the 1T phase, which is a result of a charge transfer. According to the ligand field theory (Fig. S4), the nonbonding *d*-orbitals of 2H-WS$_2$ split into three *d*-orbitals: (1) d_z^2 (filled), (2) d_{xy}, $d_{x^2-y^2}$ (empty) and (3) d_{xz}, d_{yz} (empty). An increase in *d*-electrons destabilizes the 2H WS$_2$ phase. Charge mainly accumulates on the S atoms and is depleted in the region between the S and W atoms indicating that extra electrons could weaken the W−S bonds. The distinct out-of-plane strains result in continuous changes of S-Mo-S bonding angles. Meanwhile, a small number of electrons could be transferred into the nonbonding d-orbitals of Mo, which makes WS$_2$ isoelectronic with group 7 TMDs whose nonbonding d-orbitals prefer to split into two d-orbitals: (1) d_{yz}, d_{xz}, d_{xy} (filled) and (2) d_z^2, $d_{x^2-y^2}$ (empty) and exhibit a metallic character. In this condition, an extra electron fills an unoccupied W 4d-orbital and the 1T phase is stabilized. However, d-orbitals of 1T WS$_2$ without charge transfer can be described as (1) d_{yz}, d_{xz}, d_{xy} (partially filled) and (2) d_z^2, $d_{x^2-y^2}$ (empty). The incomplete occupation of degenerate orbitals decreases lattice stability, and therefore the strain promotes the phase transition by both weakening the W−S bond and decreasing the relative energy of 1T-WS$_2$. Electrochemical impedance spectroscopy (EIS) was also performed to study the charge-transfer kinetics at the electrode/electrolyte interface. Indeed, Fig. 2e shows an obvious decrease in the charge-transfer resistance with increasing number of CV cycles implying that the semiconductor–metal transition not only provides higher catalytic activity but also facilitates the charge and mass transfer. Lastly, contact angle measurements were also performed on the WS$_2$ nanobelt films used in the HER process (Fig. 2f) which confirmed the highly hydrophilic surface of 1T-WS$_2$.

3.3. Topological transformation of WS$_2$ nanobelts in the HER process

Fig. 3a shows the twirled or twisted morphology of WS$_2$ nanobelts before and after CV cycling, which led us to hypothesize that the H$_2$ bubble may have induced strain in the WS$_2$ nanobelts and transformed them into nanohelices. The enhancement in performance is associated with a morphological evolution of the catalyst. Fig. S5 is a TEM image of a WS$_2$ nanohelix that is comprised of 8 layers, implying that nanobelts with thickness less than 8 layers can be twisted into a helix during cycling. From the results of the finite element method (Fig. 3b, Tables

S4 and S5) and the HAADF-TEM image (Fig. 3c), it can be inferred that the surface of a WS$_2$ nanohelix possess different stress states. The false colors highlight the stressed regions along the length of the nanohelix implying that strain was systematically introduced on the surface of WS$_2$ nanohelices during the topological transformation from a nanobelt to a nanohelix. Fig. 3e is the filtered image of a WS$_2$ nanohelix wherein the bright atom contrast arises from the presence of 1T-WS$_2$ phase in the individual layers of the WS$_2$ nanobelts. The presence of the 2H-WS$_2$ phase which show a lesser contrast in comparison to the 1T-WS$_2$ can be also be inferred from the image in Fig. 3e. We correlated the high contrast regions to the 1T phase from the strain values provided by the stress tensor map (Fig. 3f) of the HRTEM image (Fig. 3e). Our analysis finds that there is ~70% of 1T phase and 0~6% strain in WS$_2$ nanohelices. Using contrast, which is based on the difference in the individual atomic numbers of W and S, Fig. 3g clearly demonstrates the coexistence of 1T and 2H phases in WS$_2$ nanohelices. These findings collectively suggest that CV cycling transforms WS$_2$ from a semiconducting 2H phase to a metallic 1T phase.

3.4. Materials stability and HER enhancement mechanism

As shown in the phonon dispersion of 1T-WS$_2$ (Fig. S6a), the imaginary frequencies are large that mainly originate from the two out of three acoustic branches. The largest instability around the K point of its hexagonal lattice indicated the 1T phase is unstable at the zone border. The third branch tracks only positive frequency values in its dispersion. However, 1T-WS$_2$ phase can be stabilized by applying a biaxial strain in Fig. S6. Fig. 4a shows the phonon dispersion curves of 1T-WS$_2$ with -6% biaxial compressive strain. There are no imaginary frequencies observed completely when the biaxial compressive strain reaches -6%, which clearly implies that such nanostructures are dynamically stable. The application of a biaxial strain decreases the effective planar area of the layered WS$_2$, which significantly induces an increase in charge density. This effect is akin to charge transfer induced by the intercalation of alkali metal, which is known to stabilize 1T-WS$_2$.

The long-term stability of WS$_2$ nanobelts electrode for the HER was also evaluated in a 0.5 M aqueous H$_2$SO$_4$ solution. For comparison, the long-term stability of Pt/C electrode was also evaluated under the similar conditions. [35] Interestingly, at a current density of 10 mA cm^{-2},
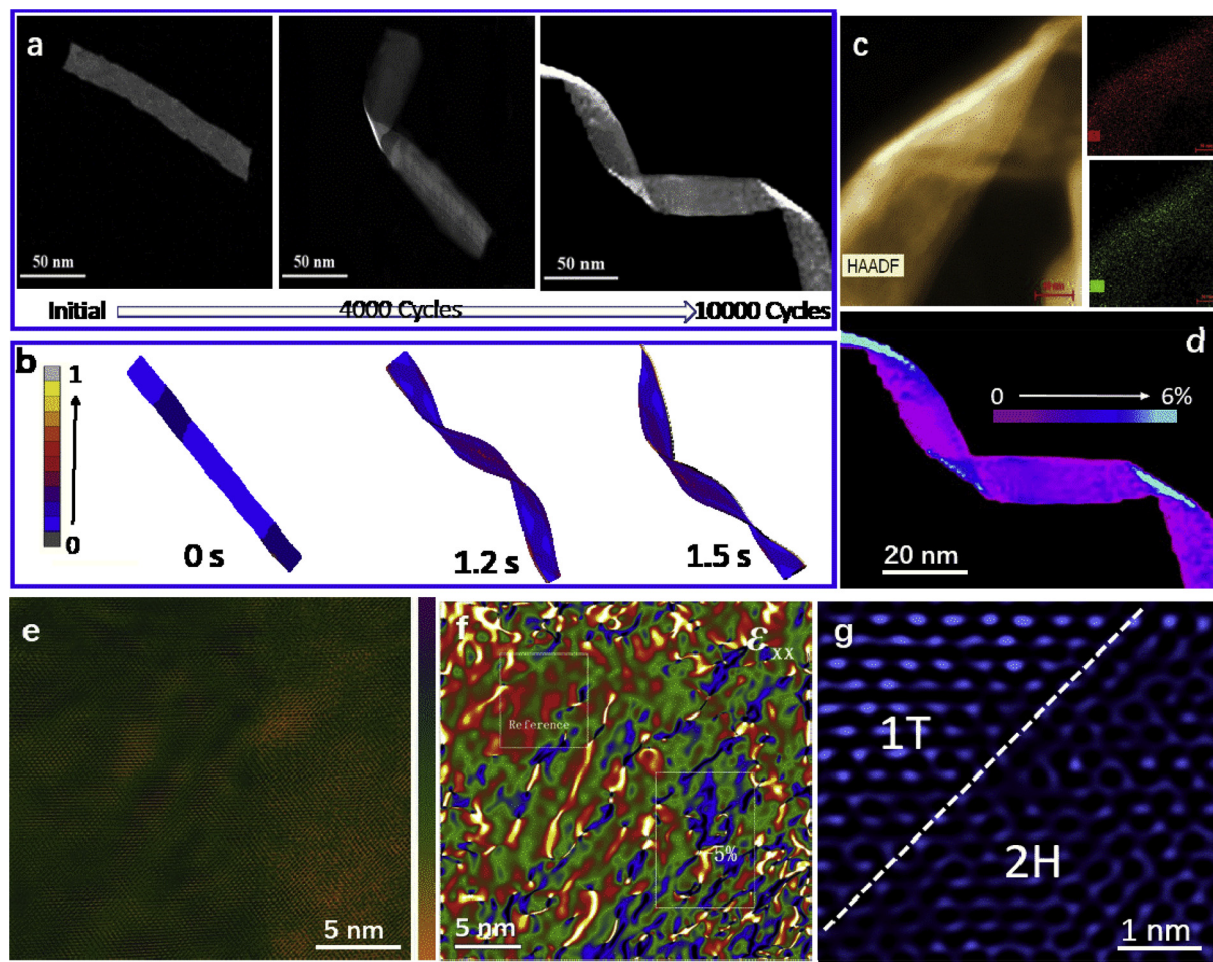
Fig. 3. Morphological and phase evolution of WS$_2$ nanobelts following cycling. (a) Morphological evolution of WS$_2$ nanobelts with increasing number of cycles. (b) Finite-element calculations of strain in nanohelices. The relative stress distribution at no twist (t = 0 s), moderate twist (t = 1.2 s), and large twist (t = 1.5 s). (c) HAADF-HRTEM and corresponding elemental mapping of cycled WS$_2$ nanobelts. (d) TEM image with false colors of a WS$_2$ nanohelices after cycling. (e) HRTEM image of a WS$_2$ nanohelice and (f) its corresponding strain map. (g) A HRTEM image of a WS$_2$ nanohelice showing its in-plane 1T –2H heterostructure.
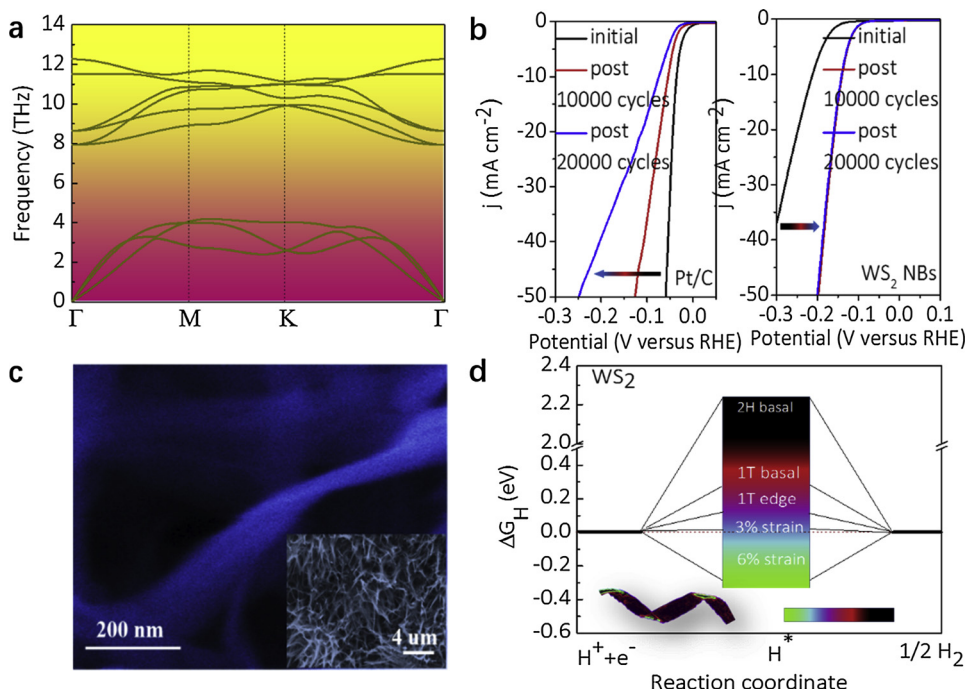

Fig. 4. (a) The calculated phonon dispersion spectrum of 1T-WS$_2$ with biaxial strain (−6%). (b) Stability test for HER of Pt/C and WS$_2$ nanobelts. The polarization curves recorded from Pt/C before and after 10,000 cycles and WS$_2$ nanobelts before and after 10,000, 20,000 potential cycles in 0.5 M H$_2$SO$_4$ solution from 0.2 to −0.2 V (versus RHE). (c) SEM image of WS$_2$ nanohelices (after WS$_2$ nanobelts were cycled for 20,000 times). (d) Comparison of the influence of different sites and strains for the 1T- and 2H-WS$_2$ phases on the HER performance. ΔG$_H$ diagram of the different H adsorption sites. The inset is a TEM image (with false color) of WS$_2$ nanohelices.

the polarization curve of Pt/C shifted negatively by about 50 mV after 20,000 cycles of continuous operation, indicating a significant decrease in its electrocatalytic activity (Fig. 4b). In striking contrast, at a current density of 10 mA cm^{-2} after 1000 cycles, the polarization curve of WS$_2$ nanobelts shifted positively by approximately 40 mV. Then, the catalyst maintains high HER activity with negligible degradation after 2000 cycles. This is a clear evidence for the excellent electrochemical stability of WS$_2$ nanobelts for long-term electrochemical processes. In addition, the stable i–t curve (Fig. S8) demonstrated a high durability of WS$_2$ under the HER conditions.

A SEM image of WS$_2$ nanobelts after 20,000 potential cycles in 0.5 M H$_2$SO$_4$ solution from 0.2 to -0.2 V (versus RHE) is shown in Fig. 4c. The WS$_2$ nanohelices are interconnected with each other and form an open porous framework, which not only exposes the active edges but also provides easy access to the reagents to the interior surfaces of the 1T-WS$_2$ electrode.

DFT calculations and comparative HER measurements were also performed to gain further insight on the influence of different phases of WS$_2$ for HER activity. The hydrogen adsorption free energy (ΔG_H) is usually used as a descriptor of the catalytic performance wherein a ΔG_H value close to zero suggests a superior HER activity due to an optimal balance between absorption and removal of hydrogen atoms at the active sites. This is attributed to the fact that if hydrogen does not efficiently bind to the catalyst, or forms a strong bond, then the proton/electron-transfer step and hydrogen release will be inefficient which decreases catalytic activity. State-of-the-art simulations indicate the crucial existence of strain to enhance the catalytic activity of WS$_2$ nanostructures. We calculated the free energy of atomic hydrogen adsorption of distorted 1T WS$_2$ monolayers with different strain and find that strain can significantly influence the ΔG_H on the surface of distorted 1T-WS$_2$ (Fig. 4d). The free energy of hydrogen adsorption is 0.23 eV in the absence of strain, which becomes close to thermoneutral value in the presence of ~3.0% strain. These results clearly indicate that the 1T WS$_2$ phase is catalytically active. For comparison, the effect of strain on the catalytic activity of 2H WS$_2$ was calculated and no improvement in catalytic activity was found. For example, even with a strain as high as 4%, the free energy remained close to ~2 eV [45]. Consequently, both electron transport and active sites are enhanced by the topotactic transformation, which act in concert to boost the overall catalytic performance. We unambiguously attribute the dramatic effect of electrochemical activation to the decreased charge transfer resistance, enhanced per site activity and an increase in the number of active sites by topological phase transition. The sulfur vacancies induced in the HER process not only contribute to the stability of 1T phase [18] but also have positive effect on the HER catalysis [46].

4. Conclusion

In summary, we successfully demonstrated the synthesis of novel 1T-WS$_2$ nanohelices by *in situ* topotactic transformation of 2H-WS$_2$ nanobelts. Our study suggests that the introduction of strain in WS$_2$ nanobelts can turn an inactive material such as 2H-WS$_2$ nanobelts into highly efficient electrocatalytic 1T WS$_2$ nanohelices for HER. By virtue of the abundant edge sites and excellent electrical transport property, such 1T-WS$_2$ nanohelices exhibited rather low Tafel slopes ˜40 mV dec^{-1} and low overpotential of 170 mV for an electrocatalytic current density of 10 mA/cm^2. This study is expected to further advance the effectiveness of topology in chemistry and materials science for realizing not only fascinating geometries of the nanostructures but also their topology-dependent catalytic properties.

Acknowledgements

Appendix A. Supplementary data

References

[1] J. Nai, J. Zhang, X.W. Lou, Construction of single-crystalline prussian blue analog hollow nanostructures with tailorable topologies, Chemistry 4 (2018) 1967–1982, https://doi.org/10.1016/j.chempr.2018.07.001.

[2] L.L. Li, S.L. Qiao, W.J. Liu, Y. Ma, D. Wan, J. Pan, H. Wang, Intracellular construction of topology-controlled polypeptide nanostructures with diverse biological functions, Nat. Commun. 8 (2017) 1276, https://doi.org/10.1038/s41467-017-01296-8.

[3] Y. Gu, E.A. Alt, H. Wang, X. Li, A.P. Willard, J.A. Johnson, Photoswitching topology in polymer networks with metal–organic cages as crosslinks, Nature 560 (2018) 65–69, https://doi.org/10.1038/s41586-018-0339-0.

[4] J.R. Dixon, S. Selvaraj, F. Yue, A. Kim, Y. Li, Y. Shen, M. Hu, J.S. Liu, B. Ren, Topological domains in mammalian genomes identified by analysis of chromatin interactions, Nature 485 (2012) 376–380, https://doi.org/10.1038/nature11082 Nature 485 (2012) 376–380.

[5] N. Han, Y. Wang, H. Yang, J. Deng, J. Wu, Y. Li, Y. Li, Ultrathin bismuth nanosheets from in situ topotactic transformation for selective electrocatalytic CO$_2$ reduction to formate, Nat. Commun. 9 (2018) 1320, https://doi.org/10.1038/s41467-018-03712-z.

[6] Z. Liu, Y. Wang, R. Chen, C. Chen, H. Yang, J. Ma, Y. Li, S. Wang, Quaternary bimetallic phosphosulphide nanosheets derived from prussian blue analogues: origin of the ultra-high activity for oxygen evolution, J. Power Sources 403 (2018) 90–96, https://doi.org/10.1016/j.jpowsour.2018.09.078.

[7] A. Kuc, T. Heine, The electronic structure calculations of two-dimensional transition-metal dichalcogenides in the presence of external electric and magnetic fields, Chem. Soc. Rev. 44 (2015) 2603–2614, https://doi.org/10.1039/C4CS00276H.

[8] L. Guan, X. Chen, Photoexcited charge transport and accumulation in anatase TiO$_2$, ACS Appl. Energy Mater. 1 (2018) 4313–4320, https://doi.org/10.1021/acsaem.8b00944.

[9] L. Liu, J. Wu, L. Wu, M. Ye, X. Liu, Q. Wang, S. Hou, P. Lu, L. Sun, J. Zheng, L. Xing, L. Gu, X. Jiang, L. Xie, L. Jiao, Phase-selective synthesis of 1T′ MoS$_2$ monolayers and heterophase bilayers, Nat. Mater. 17 (2018) 1108–1114, https://doi.org/10.1038/s41563-018-0187-1.

[10] A.P. Nayak, S. Bhattacharyya, J. Zhu, J. Liu, X. Wu, T. Pandey, C. Jin, A.K. Singh, D. Akinwande, J.F. Lin, Pressure-induced semiconducting to metallic transition in multilayered molybdenum disulphide, Nat. Commun. 5 (2014) 3731, https://doi.org/10.1038/ncomms4731.

[11] W. Du, X. Wang, X. Sun, L. Kang, F. Jiang, X. Zhang, Q. Shao, M. Dong, H. Liu, V. Murugadoss, Z. Guo, Biological cell template synthesis of nitrogen-doped porous hollow carbon spheres/MnO$_2$ composites for high-performance asymmetric supercapacitors, Electrochim. Acta 296 (2019) 907–915, https://doi.org/10.1016/j.electacta.2018.11.074.

[12] C. Tsai, K. Chan, J.K. Nørskov, F. Abild-Pedersen, Theoretical insights into the hydrogen evolution activity of layered transition metal dichalcogenides, Surf. Sci. 640 (2015) 133–140, https://doi.org/10.1016/j.susc.2015.01.019.

[13] Y. Yang, H. Fei, G. Ruan, Y. Li, J.M. Tour, Vertically aligned WS$_2$ nanosheets for water splitting, Adv. Fun. Mater. 25 (2015) 6199–6204, https://doi.org/10.1002/adfm.201502479.

[14] Y.C. Lin, D.O. Dumcenco, Y.S. Huang, K. Suenaga, Atomic mechanism of the semiconducting-to-metallic phase transition in single-layered MoS$_2$, Nat. Nanotechnol. 9 (2014) 391–396, https://doi.org/10.1038/nnano.2014.64.

[15] K.K. Amara, Y. Chen, Y.-C. Lin, R. Kumar, E. Okunishi, K. Suenaga, S.Y. Quek, G. Eda, Dynamic structural evolution of metal–metal bonding network in monolayer WS$_2$, Chem. Mater. 28 (2016) 2308–2314, https://doi.org/10.1021/acs.chemmater.6b00379.

[16] D. Voiry, H. Yamaguchi, J. Li, R. Silva, D.C. Alves, T. Fujita, M. Chen, T. Asefa, V.B. Shenoy, G. Eda, M. Chhowalla, Conducting MoS$_2$ nanosheets as catalysts for hydrogen evolution reaction, Nat. Mater. 12 (2013) 850–855, https://doi.org/10.1021/nl403661s.

[17] Y. Kang, S. Najmaei, Z. Liu, Y. Bao, Y. Wang, X. Zhu, N.J. Halas, P. Nordlander, P.M. Ajayan, J. Lou, Z. Fang, Plasmonic hot Electron Induced structural phase transition in a MoS$_2$ monolayer, Adv. Mater. 26 (2014) 6467–6471, https://doi.org/10.1002/adma.201401802.

[18] L. Cai, J. He, Q. Liu, T. Yao, L. Chen, W. Yan, F. Hu, Y. Jiang, Y. Zhao, T. Hu, Z. Sun, S. Wei, Vacancy-induced ferromagnetism of MoS2 nanosheets, J. Am. Chem. Soc. 137 (2015) 2622–2627, https://doi.org/10.1021/ja5120908.

[19] Y. Qi, Q. Xu, Y. Wang, B. Yan, Y. Ren, Z. Chen, CO$_2$-induced phase engineering: protocol for enhanced photoelectrocatalytic performance of 2D MoS$_2$ nanosheets, ACS Nano 10 (2016) 2903–2909, https://doi.org/10.1021/acsnano.6b00001.

[20] M. Yang, N.A. Kotov, Nanoscale helices from inorganic materials, Jour. Mater. Chem. 21 (2011) 6775, https://doi.org/10.1039/C0JM03028G.

[21] F.L. Deepak, R. Esparza, B. Borges, X. López-Lozano, M. Jose-Yacaman, Rippled and helical MoS2 nanowire catalysts: an aberration corrected STEM study, Catal. Lett. 141 (2011) 518–524, https://doi.org/10.1007/s10562-011-0550-1.

[22] Q. Liu, X. Li, Z. Xiao, Y. Zhou, H. Chen, A. Khalil, T. Xiang, J. Xu, W. Chu, X. Wu, J. Yang, C. Wang, Y. Xiong, C. Jin, P.M. Ajayan, L. Song, Stable metallic 1T-WS$_2$ nanoribbons intercalated with ammonia ions: the correlation between structure and electrical/optical properties, Adv. Mater 27 (2015) 4837–4844, https://doi.org/10.1002/adma.201502134.

[23] J. Luo, T. Liu, D. Zhang, K. Yin, D. Wang, W. Zhang, C. Liu, C. Yang, Y. Wei, L. Wang, S. Luo, J.C. Crittenden, The individual and Co-exposure degradation of benzophenone derivatives by UV/H$_2$O$_2$ and UV/PDS in different water matrices, Water Res. 159 (2019) 102–110, https://doi.org/10.1016/j.watres.2019.05.019.

[24] S. Li, Y.C. Lin, W. Zhao, J. Wu, Z. Wang, Z. Hu, Y. Shen, D.M. Tang, J. Wang, Q. Zhang, H. Zhu, L. Chu, W. Zhao, C. Liu, Z. Sun, T. Taniguchi, M. Osada, W. Chen, Q.H. Xu, A.T.S. Wee, K. Suenaga, F. Ding, G. Eda, Vapour–liquid–solid growth of monolayer MoS$_2$ nanoribbons, Nat. Mater. 17 (2018) 535–542, https://doi.org/10.1038/s41563-018-0055-z.

[25] T. Ling, D.Y. Yan, H. Wang, Y. Jiao, Z. Hu, Y. Zheng, L. Zheng, J. Mao, H. Liu, X.W. Du, M. Jaroniec, S.Z. Qiao, Nat. Commun. 8 (2017) 1509, https://doi.org/10.1038/s41563-018-0055-z.

[26] Z. Tian, W. Huang, B. Xu, X. Li, Y. Mei, Anisotropic rolling and controlled chirality of nanocrystalline diamond nanomembranes toward biomimetic helical frameworks, Nano Lett. 18 (2018) 3688–3694, https://doi.org/10.1021/acs.nanolett.8b00828.

[27] N.Z. Lingzheng Bu, Shaojun Guo, Xu Zhang, Jing Li, Jianlin Yao, G.L. Tao Wu, Jing-Yuan Ma, Dong Su, Xiaoqing Huang, Biaxially strained PtPb/Pt core/shell nanoplate boosts oxygen reduction catalysis, Science 354 (2016) 1410–1414, https://doi.org/10.1126/science.aah 6133.

[28] X. Li, M. Wu, B. Xu, R. Liu, C. Ouyang, Compressive strain induced dynamical stability of monolayer 1T-MX$_2$ (M = Mo, W; X = S, Se), Mater. Res. Express 4 (2017) 115018 https://iopscience.iop.org/article/10.1088/2053-1591/aa9762/meta.

[29] S.X. Haotian Wang, Charlie Tsai, Yuzhang Li, Chong Liu, Jie Zhao, H.Y. Yayuan Liu, Frank Abild-Pedersen, Fritz B. Prinz, Y.C. Jens, K. Nørskov, Direct and continuous strain control of catalysts with tunable battery electrode materials, Science 354 (2016) 1031–1036, https://doi.org/10.1126/science.aaf7680.

[30] D.Y. Hwang, D.H. Suh, Evolution of a high local strain in rolling up MoS$_2$ sheets decorated with Ag and Au nanoparticles for surface-enhanced Raman scattering, Nanotechnology 28 (2017) 025603, , https://doi.org/10.1088/1361-6528/28/2/025603.

[31] D.Y. Hwang, K.H. Choi, J.E. Park, D.H. Suh, Highly efficient hydrogen evolution reaction by strain and phase engineering in composites of Pt and MoS$_2$ nano-scrolls, Phys. Chem. Chem. Phys. 19 (2017) 18356–18365, https://doi.org/10.1039/C7CP03495D.

[32] W. Cheng, X. Zhao, H. Su, F. Tang, W. Che, H. Zhang, Q. Liu, Lattice-strained metal–organic-framework arrays for bifunctional oxygen electrocatalysis, Nat. Energy 4 (2019) 115–122, https://doi.org/10.1038/s41560-018-0308-8.

[33] M. Luo, S. Guo, Strain-controlled electrocatalysis on multimetallic nanomaterials,

[34] P. Johari, V.B. Shenoy, Tuning the electronic properties of semiconducting transition metal dichalcogenides by applying mechanical strains, ACS Nano 6 (6) (2012) 5449–5456, https://doi.org/10.1021/nn301320r.

[35] X. Li, H.-Y. Wang, H. Yang, W. Cai, S. Liu, B. Liu, In situ/operando characterization techniques to probe the electrochemical reactions for energy conversion, Small Methods 2 (2018) 1700395, https://doi.org/10.1002/smtd.201700395.

[36] L. Tian, J. Murowchick, X. Chen, Improving the activity of CoxP nanoparticles for the electrochemical hydrogen evolution by hydrogenation, Sustain. Energy Fuels 1 (2017) 62–68, https://doi.org/10.1039/C6SE00058D.

[37] L. Tian, X. Yan, X. Chen, Electrochemical activity of Iron phosphide nanoparticles in hydrogen evolution reaction, ACS Catal. 6 (2016) 5441–5448, https://doi.org/10.1021/acscatal.6b01515.

[38] L. Tian, X. Yan, X. Chen, L. Liu, X. Chen, One-pot, large-scale, simple synthesis of CoxP nanocatalysts for electrochemical hydrogen evolution, J. Mater. Chem. A Mater. Energy Sustain. 4 (2016) 13011–13016, https://doi.org/10.1039/C6TA05503F.

[39] X. Yan, K. Li, L. Lyu, F. Song, J. He, D. Niu, L. Liu, X. Hu, X. Chen, From water oxidation to reduction: transformation from NixCo$_{3-x}$O$_4$ nanowires to NiCo/NiCoOx heterostructures, ACS Appl. Mater. Interfaces 8 (2016) 3208–3214, https://doi.org/10.1021/acsami.5b10724.

[40] X. Yan, L. Tian, S. Atkins, Y. Liu, J. Murowchick, X. Chen, Converting CoMoO4 into CoO/MoOx for overall water splitting by hydrogenation, Eng. ACS Sustain. Chem. 4 (2016) 3743–3749, https://doi.org/10.1021/acssuschemeng.6b00383.

[41] X. Yan, L. Tian, X. Chen, Crystalline/amorphous Ni/NiO core/shell nanosheets as highly active electrocatalysts for hydrogen evolution reaction, J. Power Sources 300 (2015) 336–343, https://doi.org/10.1016/j.jpowsour.2015.09.089.

[42] X. Yan, L. Tian, M. He, X. Chen, Three-dimensional crystalline/amorphous Co/Co3O4 core/shell nanosheets as efficient electrocatalysts for the hydrogen evolution reaction, Nano Lett. 15 (2015) 6015–6021, https://doi.org/10.1021/acs.nanolett.5b02205.

[43] X. Yan, L. Tian, K. Li, S. Atkins, H. Zhao, J. Murowchick, L. Liu, X. Chen, FeNi3/NiFeOx nanohybrids as highly efficient bifunctional electrocatalysts for overall water splitting, Adv. Mater. Interfaces 3 (2016), https://doi.org/10.1002/admi.201600368.

[44] J.Y. Zhang, H.M. Wang, Y.F. Tian, Y. Yan, Q. Xu, T. He, H.F. Liu, C.D. Wang, Y. Chen, B.Y. Xia, Anodic hydrazine oxidation assists energy-efficient hydrogen evolution over bifunctional cobalt perselenide nanosheet electrode, Angew. Chem. Int. Ed. 57 (2018) 7649–7653, https://doi.org/10.1002/anie.201803543.

[45] H. Yuan, L. Kong, T. Li, Q. Zhang, A review of transition metal chalcogenide/graphene nanocomposites for energy storage and conversion, Chin. Chem. Lett. 28 (2017) 2180–2194, https://doi.org/10.1016/j.cclet.2017.11.038.

[46] X. Zhao, X. Ma, J. Sun, D. Li, X. Yang, Enhanced catalytic activities of surfactant-assisted exfoliated WS$_2$ nanodots for hydrogen evolution, ACS Nano (2016) 2159–2166, https://doi.org/10.1021/acsnano.5b06653.

Nat. Rev. Mater. 2 (2017) 17059, https://doi.org/10.1038/natrevmats.2017.59.